Atmospheric Environment 44 (2010) 512–522

Contents lists available at ScienceDirect

Atmospheric Environment

journal homepage: www.elsevier.com/locate/atmosenv

Comparison of a two-dimensional numerical dust transport model with experimental dust emissions from soil surfaces in a wind tunnel

Jason A. Roney [a,*], Bruce R. White [b]

[a] ITT Corporation, 5009 Centennial Blvd, Colorado Springs, CO 80919, USA
[b] Department of Mechanical and Aeronautical Engineering, One Shields Avenue, University of California, Davis, CA 95616, USA

ARTICLE INFO

Article history:
Received 7 July 2009
Received in revised form
23 October 2009
Accepted 29 October 2009

Keywords:
Particulate matter
Fugitive dust
Aerosols
Advection
Diffusion
Numerical model

ABSTRACT

Near-surface wind-tunnel fugitive dust concentration profiles arising from soil surfaces beds were compared to a finite difference numerical dust transport model. Comparisons of the type shown in this study were previously non-existent in the literature due to the lack of experimental wind-tunnel data for near-surface concentrations over a soil bed. However, in a previous study by the authors, near-surface steady-state concentration profiles were measured in order to obtain fugitive dust emission rates, thus allowing the comparison to models shown in this paper. The novel aspects of the current study include: comparison of concentration profiles of dust obtained experimentally in the wind tunnel with those calculated numerically; comparison of the calculated numerical fetch effect on dust emissions with that obtained in the wind tunnel; and comparison of the emission rates calculated numerically with those obtained experimentally in the wind tunnel. Initial comparisons with the model indicate good agreement implying that the physical mechanism of advection–diffusion is reasonably modeled with the choice of equations for the simple "steady-state" process near the surface. Furthermore, the numerical solutions presented in this paper provide a means to systematically explore the relative impact of varied surface boundary conditions upon the emission process and provide a potential link between wind-tunnel simulations and field scale models.

1. Introduction

This study is aimed at building knowledge describing the potential fugitive dust emissions at soil surfaces. It is a first step in developing a piece-wise progression of models that may lead to larger scale models. By first studying "simple" predictive mathematical and numerical models, which simulate the physics of advection–diffusion of dust within the wind tunnel at the soil–air interface, confidence can been gained in simulating the near-surface dynamics where dust generation begins. Since measurement of concentration profiles at multiple downwind locations is rare, simple models which can predict concentration profiles have never previously been compared to any physical data of dust (PM_{10}) near the surface. By using these initial insights and incorporating realistic atmospheric dynamics more sophisticated emission rate models may be developed. More importantly, this methodology could be used as a means to estimate full-scale field fugitive dust emission rates at specific sites. However, the immediate objective of the numerical model comparisons presented in this paper is to provide physical interpretation and knowledge of the fundamental transport near the surface.

2. Background

One of the original studies mathematically describing the concentration profiles of dust in the atmosphere is by Gillette and Goodwin (1974). They used an Eulerian Pasquill equation as the representative equation for this process as given by Pasquill (1962):

$$\frac{\partial c}{\partial t} + \vec{\nabla}\cdot(c\vec{v}) = \vec{\nabla}\cdot(\vec{\vec{D}}\cdot\vec{\nabla}c) - \vec{w}\cdot\vec{\nabla}c, \tag{1}$$

where $c(x, y, z, t)$ is the mean concentration of the sand or soil aerosol, $\vec{v}(x,y,z)$ is the mean velocity of the wind, $\vec{w}(x,y,z)$ is the settling velocity vector, and $\vec{\vec{D}}(x,y,z)$ is the spatial diffusion tensor. In their study, they postulated the existence of "an atmospheric layer of arbitrary thickness" (the surface layer), such that the wind and diffusivity profiles may be described in an average sense by certain well-behaved functions that have been found representative of the region. The diffusivity is then given by the following expression as a function of height above the ground:

$$D(z) = \lambda z = u_* k z, \quad \text{where } u_* = \left(\frac{\tau_\omega}{\rho}\right)^{1/2}, \tag{2}$$

* Corresponding author. Tel.: +1 719 599 1590; fax: +1 719 599 1799.
E-mail address: Jason.Roney@itt.com (J.A. Roney).

1352-2310/$ – see front matter © 2009 Elsevier Ltd. All rights reserved.
doi:10.1016/j.atmosenv.2009.10.046

where u_* is the friction velocity, k is the von Karman constant, $\lambda = u_* k$ and τ_ω is the surface shear stress. Gillette and Goodwin (1974) assumed steady-state conditions, and homogeneity of c in the x- and y-direction to give the following simplified equation:

$$\frac{\partial}{\partial z}\left(D_z \frac{\partial c}{\partial z}\right) - w\frac{\partial c}{\partial z} = 0, \tag{3}$$

where w is the settling velocity in the z-direction, and D_z is the turbulent diffusivity in the z-direction. The equation becomes simply a balance between gravitational settling and the vertical turbulent diffusion. The equation can be solved to yield the following result:

$$c(z) = c(z_0)\left(\frac{z}{z_0}\right)^{-\xi} \tag{4}$$

$$\lim_{z\to\infty}(c(z)) = 0,$$

$$c(z)|_{z=z_0} = \text{const}$$

where z_0 is the roughness height and $\xi = w/(ku_*)$. This function was a first attempt to describe the concentration profile of dust or sand in the atmosphere, and is still widely used in field studies to fit limited data. However, it is known not to be entirely accurate, since in atmospheric flows, winds are unsteady over time and concentrations vary spatially in the x- and y-directions. A major assumption in Equation (4) is also that x (the downwind length) has approached infinity.

Hassan and Eltayeb (1991a) presented a mathematical model based on the Eulerian diffusion equation of Pasquill (1962) to extend the analysis of Gillette and Goodwin (1974). The Pasquill model (Equation (1)) was simplified by Hassan and Eltayeb to obtain an equation which could be solved analytically and did not have as many limitations on applicability as the Gillette and Goodwin model. The simplified equation is steady state, the settling velocity is directed downward and is only a function of the particle diameter, and the concentration and the diffusion tensor are taken as homogenous in the y-direction. The windward transport is assumed stronger than the turbulent transport in the same direction. These assumptions lead to the following simplified equation:

$$U\frac{\partial c}{\partial x} = \frac{\partial}{\partial z}\left(D_z\frac{\partial c}{\partial z}\right) + w\frac{\partial c}{\partial z} \text{ or } U\frac{\partial c}{\partial x} = D_z\frac{\partial^2 c}{\partial z^2} + (\lambda + w)\frac{\partial c}{\partial z}, \tag{5}$$

where U is the streamwise "steady-state" velocity which is a function of z-only ($U(z) = \beta z^m$, where β and m are constants), D_z is Diffusion coefficient in the z-direction, and w is the downward settling velocity of a dust particle. All of these assumptions are especially reasonable assumptions for dust transport in the wind tunnel as well. D_z is modeled as the turbulent diffusivity as in Gillette and Goodwin (1974) and given in Equation (2).

Even after simplification, the above equation has no exact solution unless very specific boundary conditions are applied. When the specific boundary conditions are applied, the Partial Differential Equation can be transformed into an Ordinary Differential Equation, and solved analytically. In Hassan and Eltayeb (1991a) and Eltayeb and Hassan (1992) analytical solutions were presented for two specific types of boundary conditions. The first type of boundary conditions for which the equations were solved is the following:

$$\begin{aligned} &\text{(i) } c(0,z) = F(z)\\ &\text{(ii) } c(\infty,z) = 0.0\\ &\text{(iii) } c(x,\infty) = 0.0. \end{aligned} \tag{6}$$

The functional form $F(z)$ of boundary condition (i) is similar to Equation (4). The exponent is modified slightly, and below z_0 there is a restriction placed on the concentration:

$$\begin{aligned} &F(z) = c(z) = c(z_0)\left(\frac{z_0}{z}\right)^{\nu} \quad \text{if } z \geq z_0\\ &F(z) = c(z) = 0 \quad \text{if } z \leq z_0\\ &\text{where } \nu = \frac{w}{\lambda(m+1)}. \end{aligned} \tag{7}$$

The functional form of the boundary conditions represents a pre-existing concentration profile which decays away from the surface towards zero for increasing height in the atmosphere. Boundary condition (ii) indicates that the concentration profile in the atmosphere approaches zero far downwind of the profile. Likewise, boundary condition (iii) indicates that at infinite heights in the atmosphere, the concentration is zero matching boundary condition (i). However, this specific problem is not representative of the wind-tunnel experiments presented in Roney and White (2006). Instead, this case represents the diffusion of a decaying concentration profile with no other additional sources or sinks.

At the end of the article, Hassan and Eltayeb (1991a) mention that colleagues have suggested obtaining a solution to the following boundary conditions:

$$\begin{aligned} &\text{(i) } c(0,z) = 0.0\\ &\text{(ii) } c(x,\infty) = 0.0\\ &\text{(iii) } c(x,0) = F(x). \end{aligned} \tag{8}$$

In this case, boundary condition (i) represents no initial upwind dust concentrations; boundary condition (ii) represents the extinction of dust at infinite heights; and (iii) represents the surface concentration as a function of streamwise distance. More interestingly, these boundary conditions are reasonable representations of the conditions in the wind-tunnel studies performed by Roney and White (2006).

Following colleagues' suggestions, Eltayeb and Hassan (1992) solved the above problem for the specific boundary conditions with a Laplace transform. The boundary conditions are formulated as the following in their problem:

$$\begin{aligned} &\text{(i) } c(0,Z) = 0.0\\ &\text{(ii) } c(X,\infty) = 0.0\\ &\text{(iii) } c(X,Z_0) = c_0 g(X) \end{aligned} \tag{9}$$

where Z, and X are transformed variables. The variables are defined as the following

$$\begin{aligned} Z &= z^{(m+1)/2}\\ X &= \frac{\lambda(m+1)^2}{4\beta}x \end{aligned} \tag{10}$$

where the variables x, z, m, β, ν and λ are as previously defined. In this case, $g(X)$ is a concentration boundary-profile function, and c_0 is a constant concentration value. For $g(X) = 1$, a complete analytical Laplace transform solution is possible:

$$c(X,Z) = c_0\left(\frac{Z_0}{Z}\right)^{2\nu}\frac{\Gamma\left(\nu, Z^2/4X\right)}{\Gamma(\nu)}, \quad Z_0 \to 0, \tag{11}$$

where $\Gamma(\nu, Z^2/4X)$ is the incomplete Gamma function and $\Gamma(\nu)$ is the Gamma function. A second profile Eltayeb and Hassan suggest is $g(X) = Xe^{-x/\alpha}$ where α represents a decay factor; however, they were unable to find an analytical solution for this form of the function, but instead numerically integrated to arrive at a solution.

The analytical approach provides solutions to hypothetical problems; however, the choices for the boundary profiles are not substantiated with any physical measurement nor is there any

comparison to experimental data. Eltayeb and Hassan (1992) acknowledge in their concluding remarks, "to our knowledge no observational data related to the simultaneous measurement of dust distribution in the vertical and downwind directions is available and we hope that the results published here will stimulate others to carry out these measurements". The types of measurement necessary for these types of comparison were conducted in the experimental phase of a larger study by Roney and White (2006). The experiments are thus compared to a numerical model that is based on the physical arguments of Eltayeb and Hassan (1992) and presented in this paper.

3. Numerical modeling approach

An alternative to analytical modeling is a finite difference numerical solution of the simplified equations presented by Eltayeb and Hassan (1992). The numerical model provides solutions to all the types of problems presented by Hassan and Eltayeb (1991a,b, 1993) and Eltayeb and Hassan (1992), while allowing exploration of boundary conditions that do not lend to analytical solutions. However, a caution with numerical models is that they are only simplified representations of the partial differential equations and are subject to approximation error, numerical diffusion error, and stability criteria. Efforts to minimize these effects were considered in our formulation and solutions. The physical assumptions previously posed by Eltayeb and Hassan and leading to Equation (5) correspond to the "steady-state" wind-tunnel conditions in Roney and White (2006). Thus, a finite difference model of Equation (5) was used to study multiple boundary profiles and initial concentration profiles. In the finite difference formulation, the steady-state velocity field was not limited to the power-law formulation, and the code results could be directly compared to physical measurements of wind-tunnel dust concentrations by using the actual surface boundary concentrations and velocity profiles from the experiments.

The numerical model is a finite difference model which uses a Crank–Nicolson scheme as presented in Jacobson (1999) and is adapted to solve Equation (5) as follows:

$$\overline{\overline{A}}_j C_{i,j-1} + \overline{\overline{B}}_j C_{i,j} + \overline{\overline{D}}_j C_{i,j+1} = \overline{\overline{E}}_j C_{i-1,j-1} + \overline{\overline{F}}_j C_{i-1,j} + \overline{\overline{G}}_j C_{i-1,j+1}$$

where,

$$\overline{\overline{A}}_j = \mu_c\left(\frac{\Delta x}{2\Delta z}\frac{(u_* k + w)}{U_j} - \frac{\Delta x}{\Delta z^2}\frac{z_j u_* k}{U_j}\right),$$

$$\overline{\overline{B}}_j = 1 + \mu_c\left(\frac{2\Delta x}{\Delta z^2}\frac{z_j u_* k}{U_j}\right),$$

$$\overline{\overline{D}}_j = -\mu_c\left(\frac{\Delta x}{\Delta z^2}\frac{z_j u_* k}{U_j} + \frac{\Delta x}{2\Delta z}\frac{(u_* k + w)}{U_j}\right),$$

$$\overline{\overline{E}}_j = (1-\mu_c)\left(\frac{\Delta x}{\Delta z^2}\frac{z_j u_* k}{U_j} - \frac{\Delta x}{2\Delta z}\frac{(u_* k + w)}{U_j}\right),$$

$$\overline{\overline{F}}_j = 1 - 2(1-\mu_c)\left(\frac{\Delta x}{\Delta z^2}\frac{z_j u_* k}{U_j}\right),$$

$$\overline{\overline{G}}_j = (1-\mu_c)\left(\frac{\Delta x}{\Delta z^2}\frac{z_j u_* k}{U_j} + \frac{\Delta x}{2\Delta z}\frac{(u_* k + w)}{U_j}\right), \tag{12}$$

where C is the concentration, Δx is the x-direction spatial discretization, Δz is the z-direction spatial discretization, and μ_c is the Crank–Nicolson parameter ($\mu_c = 0.5$ for Crank–Nicolson scheme, $\mu_c = 1.0$ for the implicit scheme, and $\mu_c = 0.0$ for the explicit Euler scheme). The settling velocity of a dust particle w is estimated as follows as given in Seinfeld and Pandis (1998):

$$w = \frac{d_p^2 \rho_p g C_c}{18\mu}, \tag{13}$$

where d_p is the diameter of the particle, ρ_p is the particle density, g is the gravitational constant, C_c is the slip correction factor for very small particles, and μ is the air viscosity. For PM_{10} sized particles w becomes very small and can be considered negligible for the wind-tunnel length; however, w is included so the model can be adapted for slightly larger dust particles.

The velocity profiles are of the following type:

$$U_j = \frac{u_*}{k}\ln(z_j/z_0') \quad \text{for } z_0' < z < \delta$$
$$U_j = U_{\max}, \quad \text{for } z > \delta, \tag{14}$$

where z_0' is effective roughness during saltation, and U_j is the "steady-state" wind velocity. U_j reaches a maximum $U_{\max}$ at the boundary layer height $z_j = \delta$. The boundary conditions for the steady-state numerical equations are the following where H_t is modeling domain height:

$$\begin{aligned} &\text{(i) } c(0,z) = 0.0 \\ &\text{(ii) } c(x,0) = F(x) \\ &\text{(iii) } c(x,H_t) = 0.0. \end{aligned} \tag{15}$$

The finite difference form of the model is semi-implicit, which is second-order accurate in both spatial directions. This time-stepping scheme with "x as the time step" also has a stability criterion associated with the time scales of advection to diffusion. The ratio of the diffusion time scale to the advection time scale is as follows:

$$\mu_c \frac{u_* k z_{\max}}{U_{\max}}\left(\frac{\Delta x}{\Delta z^2}\right) \le 1. \tag{16}$$

Within the domain size of the wind tunnel, this stability criterion was met, and due to the second-order accuracy of the scheme, numerical diffusion was limited.

The horizontal flux of emissions and the concentration profiles in a control volume are obtained with the numerical simulation in order to match the experimental cases in Roney and White (2006). In the wind tunnel, the control volume is the box representing the length of the soil bed, its width, and the height of the tunnel. The friction velocity u_*, velocity profiles $U(z)$, and surface boundary concentrations C_0 were all measured in the wind tunnel and are used to develop input for the model. These values allow numerical calculation of concentration profiles at the same locations numerically as those measured experimentally. In addition, vertical contours of the concentration from the numerical solution are plotted. The input shape of the velocity profile takes into account modification due to saltation and incorporates slip near the wall between z_0' and $z_0' + \Delta z$ such that the velocity at z_0' is the value given at $z_0' + \Delta z$. This type of profile also avoids an infinite result (division by zero) in the finite difference equations. For the wind-tunnel cases, the experimental profiles reach a maximum at the boundary layer height δ which is approximately at $z \approx 0.25$ m. The velocity profile input into the numerical code takes the boundary layer height effect into account as well. The diffusion coefficient is taken as constant above the boundary layer, $D_z = u_* k \delta$.

PM_{10} size particles measured in the experiments are assumed coarse mode particles (produced by mechanical means as compared to chemical means); therefore, the distribution of sizes is estimated as those shown in Seinfeld and Pandis (1998) for the coarse mode. As a first-order approximation, the mean diameter of the distribution is taken as 5.0 μm. The particles measured experimentally by the aerosol sampler in the experiments are 10.0 μm or less.

3.1. Constant concentration boundary condition

As a first approach, the function $F(x)$ along the surface boundary is considered constant and is estimated from the near-surface

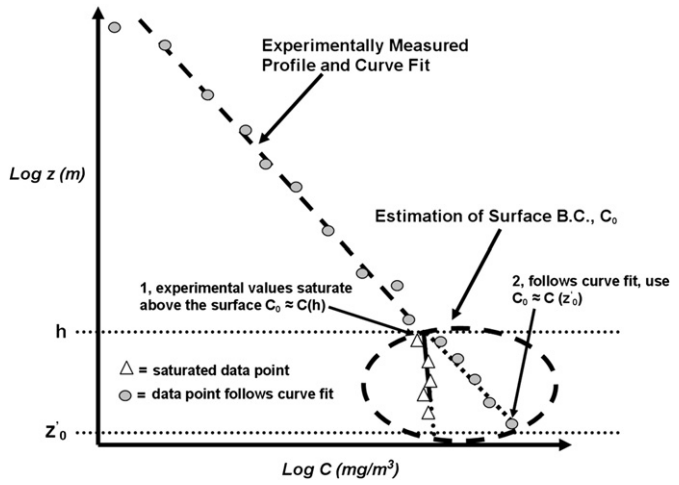

Fig. 1. Estimates of the surface boundary condition C_0 for input into the numerical model were found from the experimental data by (1) extending the saturation line or (2) extending the general trend line.

concentration values obtained experimentally as shown in Fig. 1. A good first approximation is that the entire soil bed emits the same amount very near surface under equivalent shear conditions. The solution domain is related to the physical dimensions of the actual experimental set-up; and, therefore, $x = 0.0$–5.0 m and $z = z_0'$–0.50 m. The initial condition is that all values of concentration other than the surface boundary are considered zero. The soil density is taken as that of a silica particle, 2.65 g cm^{-3} (2650 kg m^{-3}), and the settling velocity w is considered to follow the Stokes' regime for small particles. The settling velocity for this case is very small ≈ 0.0024 m s^{-1}. In addition, the emission rate and horizontal flux is calculated in the same way numerically as experimentally in Roney and White (2006) to obtain direct comparison (i.e., integrated between $z = 0.01$ m and $z = 0.50$ m). The range of input variables were the following: $z_0' = 0.0001$–0.001 m, $u_* = 0.35$–1.10 m s^{-1}, and $C_0 = 1.0$–180.0 mg m^{-3}, corresponding to various experimental conditions.

3.2. Step-function surface boundary condition

A step-function boundary conditions was used to simulate the North and South Sheet experiment simulations described in Roney and White (2006) which were composed of a non-homogenous bed (in terms of soil type) with sand soil placed upwind of a "loamy-type" soil. Two constant surface boundary conditions were designated for this case $F(x) = C_{01}$ for the sand soil and $F(x) = C_{02}$ for the loamy soils. More formally, the surface boundary condition is written as follows:

$$\begin{aligned} F(x) &= \{C_{01} \quad \text{for } 0 \le x < 2.65 \\ F(x) &= \{C_{02} \quad \text{for } 2.65 \le x \le 5.0. \end{aligned} \tag{17}$$

C_{01} for the sand soil was estimated from the experimental data either through a saturation region (Case 1 if present) or through the curve fits (Case 2) as shown in Fig. 1. C_{02} for the loamy soils was estimated from the experimentally measured values at $x = 4.38$ m to represent a surface boundary condition produced by both shear and impacting sand particles. The C_{02} boundary condition typically represented higher surface level concentrations. However, in the experimental cases it was shown that the upwind "sand" in the South Sheet simulation had a considerable amount of fugitive dust as well, possibly only slightly less than the loamy soil.

3.3. Exponential decaying surface boundary condition

Different functional form boundary conditions were explored in an effort to further utilize the numerical scheme to better explain the physics of dust movement. For this case an exponential decaying function along the surface boundary was considered. The proposed physical mechanism this condition represents is a decrease in the effective shear at the surface as more and more dust and sand-size particles are entrained near the surface. The energy of the flow is depleted by the surface friction as well as by the suspended particulate in the control volume that is increasing along the fetch. The mass effect decreases the ability of the flow to suspend the same amounts of dust near the surface of the homogenous (same soil) bed. To represent this condition, the boundary conditions explored were of the following form:

$$F(x) = C_0 e^{(\alpha x)}, \tag{18}$$

where C_0 is the initial concentration at z_0' directly resulting from the shear before substantial mass loading near the surface occurs, and α is a negative constant representing the effect of mass loading downwind. When there is minimal mass in the air $\alpha \to 0$, the boundary condition reverts back to the constant surface boundary condition. For cases in which mass loading has an effect, α becomes increasingly negative. A full numerical solution for three different α values, $\alpha = 0.0$, $\alpha = -0.25$ and $\alpha = -0.50$ is shown in the results.

3.4. Sinusoidal surface boundary condition

The sinusoidal type boundary condition is another possible functional form of the surface boundary condition. This type of boundary condition corresponds to ripples or ridges formed in the soil or sand after an initial "steady-state" sorting as described in Bagnold (1941). The assumption is that the sand particles tend to be on the ridges while the fine-grained soils tend to be in the troughs. Though these formations are steady, sand still migrates across the bed, and the turbulent nature of the flow still penetrates the troughs. Thus, the troughs of fine soils are not fully protected from saltating sand and turbulent flow. The emissions from the ripples, thus, can be estimated with sinusoidal forms, where for the simplest case the form can be estimated as follows:

$$F(x) = \frac{1}{2} C_0 \left(1 - \mathrm{Sin}\left(\frac{2\pi x}{\lambda_r}\right)\right), \tag{19}$$

where C_0 is representative of the most emissive condition, and λ_r is representative of the wavelength of the ripple pattern. The maxima represent the troughs and high emissions values, while the minima represent the top of the ridges and the lowest emissions due to their larger proportion of sand particles. Numerical cases for this boundary condition were examined for $\lambda_r = 0.2$ m, $\lambda_r = 0.5$ m, and $\lambda_r = 2.0$ m. Physically, this wavelength range might represent ordinary ripples in well sorted, medium sand to typically granular or megaripples in poor sorted sand as described in Pye and Tsoar (1990).

3.5. Combined surface boundary condition

Finally, a combined exponential and sinusoidal boundary condition was formed as follows:

$$F(x) = \frac{1}{2} C_0 e^{(\alpha x)} \left(1 - \mathrm{Sin}\left(\frac{2\pi x}{\lambda_r}\right)\right), \tag{20}$$

where all the terms are as previously defined. Now, for this boundary condition one accounts for both ripples and mass loading effects with fetch. One could imagine that the ripples are being

built downstream containing ridges with increasing amounts of sand, in effect, depleting the amount of fine emissive soils exposed to the wind shear. Or, the ripples are steady, but a mass loading effect is preventing entrainment of fine particles from the troughs downstream.

4. Numerical modeling results

4.1. Convergence and stability of the numerical scheme

Before any numerical results were compared to the experiments, test cases were run to verify convergence and stability of the scheme for the boundary condition $F(x) = C_0$. The solutions presented in the next section have both converged and are stable given the criterion set by Equation (16).

4.2. Comparisons with analytical solutions

First, the numerical solution was compared to the analytical solution of Eltayeb and Hassan (1992) for a constant surface boundary condition as in Equation (11) and to Gillette and Goodwin (1974) Equation (4). However, the upper boundary condition differs in the numerical solution in that infinity cannot be attained and a finite z must be specified. Also, since the analytical solution is only facilitated with the power-law velocity profile, the power-law velocity profile was input into the numerical solution for comparison purposes. The following parameters were used as the input for all the numerical solution test cases and in Equations (4) and (11): $z_0' = 0.0001$ m, $u_* = 0.80$ m s^{-1}, $C_0 = 50.0$ mg m^{-3}, $w = 0.0024$ m s^{-1}, $\beta = 14.277$, $m = 0.2244$. The concentration profiles were evaluated at $x = 5.0$ m. The Gamma and Incomplete Gamma functions in Equation (11) were obtained by using standard numerical subroutines that calculated the functions. Finally, the concentrations for the three methods as a function of height z at $x = 5.0$ m are shown in Fig. 2.

The analytical method of Eltayeb and Hassan (1992) has the same solution form as the numerical solution (i.e., the curves have similar trends); however, the predictions of concentrations are dramatically different between the two. However, the solution of Eltayeb and Hassan appears to be inappropriate for PM_{10} particles sizes as the constant parameter ν defined previously in Equation (7) becomes very small ($\nu \approx 0.005$) giving large values when evaluated in the Gamma Function $\Gamma(\nu) \approx 200$. Likewise, the Incomplete Gamma Function $\Gamma(\nu, Z^2/4X)$ is small except for when $Z = 0$ where it reverts to the Gamma Function. Thus, the ratio of the Incomplete Gamma Function to the Gamma Function is always much less than one for this case, except when $Z = 0$. This ratio creates a large difference between the concentrations as $z \to 0$ and $z = 0.01$. The non-physical result thus seems to be an artifact of the Gamma Function solutions which are highly non-linear at small values of the independent variable.

For larger dust particles, $d_p = 50.0$ μm for instance, the constant parameter ν will be larger and the solution of Eltayeb and Hassan is more appropriate because the Incomplete Gamma Function is of the same order as the Gamma Function for all values of $Z^2/4X$. These are the types of solutions which are shown in Eltayeb and Hassan (1992) with $\nu \approx 1.0$. For the larger particles, the numerical solution presented in this paper shows a discontinuous jump from $z = 0.0001$ m–0.01 m due to the discrete solution method. But, the values of the numerical solution are between the two analytical solutions for values calculated above $z = 0.01$ m.

A simple way to circumvent the small particle problem in the analytical solution is to use an approximate solution $\Gamma(\nu) \to \Gamma(\nu, Z_0^2/4X)$ and require $Z \geq Z_0$:

$$c(X,Z) = c_0\left(\frac{Z_0}{Z}\right)^{2\nu}\frac{\Gamma\left(\nu, Z^2/4X\right)}{\Gamma\left(\nu, Z_0^2/4X\right)}. \tag{21}$$

Though, the solution is no longer an exact solution to the partial differential equation, it represents a good approximation for those cases in which Z_0 and ν are small. The results of using this approximation are shown Fig. 3. The differences are on the order of

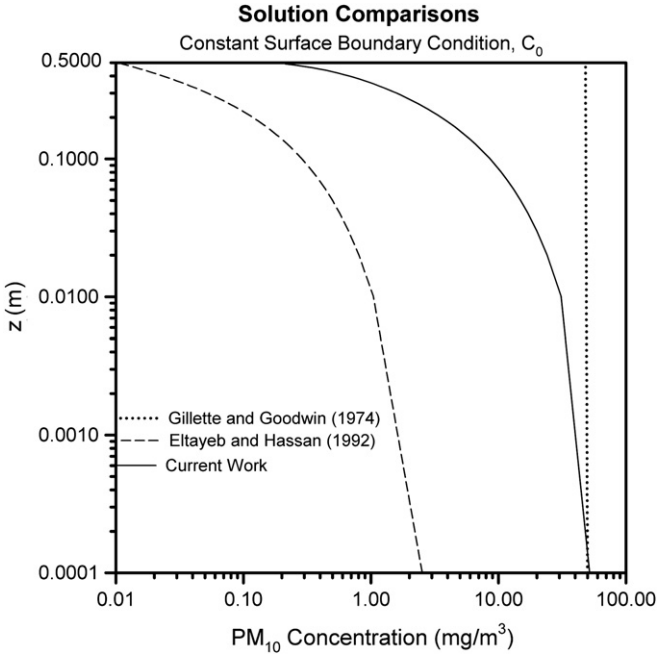

Fig. 2. Solution comparisons for three different methods for obtaining the concentration profiles for constant C_0 surface boundary conditions at $x = 5.0$ m: 1) numerical (Current Work) 2) analytical Gillette and Goodwin (1974), and 3) analytical Eltayeb and Hassan (1992).

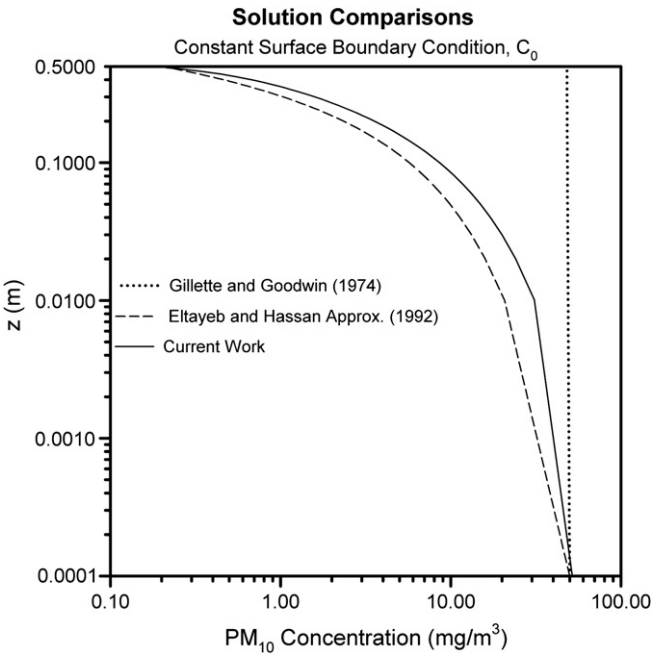

Fig. 3. Solution comparisons for three different methods for obtaining the concentration profiles for constant C_0 surface boundary conditions at $x = 5.0$ m: 1) numerical (Current Work), 2) analytical Gillette and Goodwin (1974), and 3) the analytical approximate form based on Eltayeb and Hassan (1992).

50% for the calculated horizontal flux when compared to the numerical solution. The approximation is a vast improvement for the small particles. Both the numerical and analytical solutions appear to be very slowly approaching Gillette's hypothetical solution which is valid only for $x \to \infty$. At $x = 5.0$ m in the wind-tunnel experiments, as expected, Gillette and Goodwin's solution is not valid. The numerical solution and Eltayeb and Hassan's analytical solution provide a better model for what one should expect when measuring the wind-tunnel concentration profiles. The numerical solutions are then compared to the experimental data for the constant surface boundary condition in the next section.

4.3. Constant surface boundary condition, $F(x) = C_0$

As a first approach, the function $F(x)$ along the surface boundary is considered constant and is estimated from the near-surface value obtained experimentally. Linear curve fits as a function of the shear stress were also fit to the experimental PM_{10} concentration surface data such that the curve fit could be used to fit the intermediate values that were not obtained experimentally. The assumption is that the entire soil bed acts as a homogenous source (same soil). The near-surface steady-state shear $\sim u_*^2$ acts to expel a certain mass per unit volume (concentration) of small particles near the surface creating the source. The experimental values of C_0, u_*, and z_0' were used to estimate the input for the numerical models. The numerical emission rates and concentration profiles were then compared to the experimental cases. Only the numerical emission rate values which directly simulate experimental cases were calculated. The numerical and measured emission rates compare favorably as shown in Fig. 4. Complete details of the soils types, collection sites, and the experiments are found in Roney and White (2004) and Roney and White (2006). The biggest differences in the comparisons occur with the most emissive soils (Soil #1 and Soil #4) at the highest u_* values. The differences are likely due to changing downwind boundary conditions that are noted in Roney and White (2006), and explored numerically later in this paper.

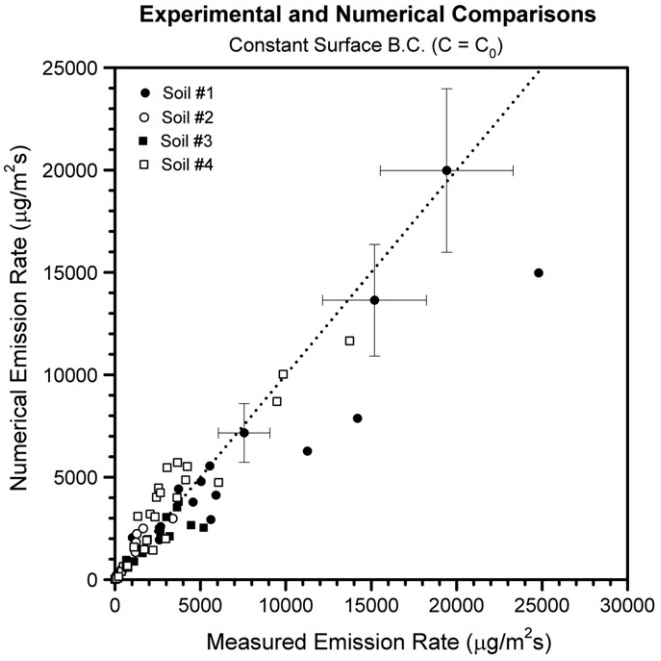

Fig. 4. Comparison of the numerical emission rate and measured emission rate for all four soils for which emission rates were measured in Roney and White (2006).

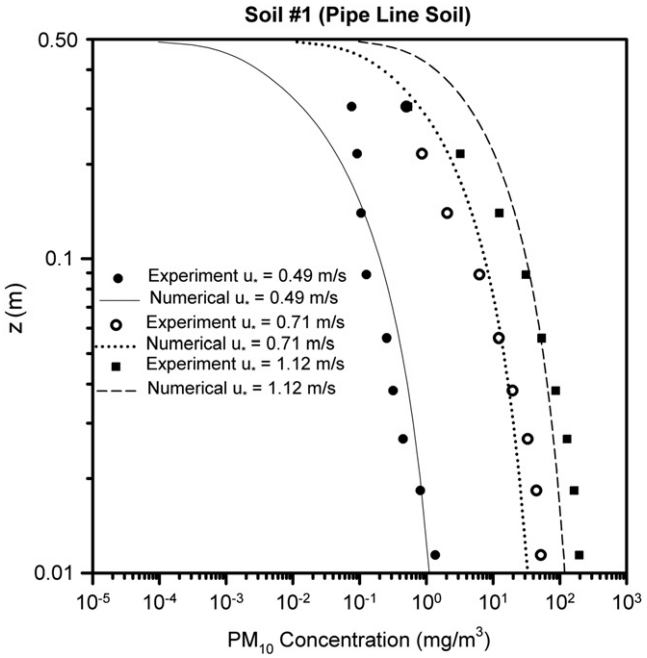

Fig. 5. Concentration profiles at $x = 4.38$ m for the numerical calculation with C_0 as a constant surface boundary condition shown with the equivalent experimentally measured concentration profiles for Soil #1.

A series of numerical concentration profiles were compared to the experimental case for each soil at $x = 4.38$ m. A sample concentration profile comparison is shown in Fig. 5. The concentration profiles compare quite well qualitatively. The only exceptions are the North Sand (Soil #2) and at some of the higher z-values in all the profiles. For the North Sand experimental results, a time dependency issue is possibly the reason that the profiles do not match as well. For the sand, the near-surface concentration values dropped to about half their original value during an experimental test that assumed "steady-state" conditions. This indicates that the last points taken in the profile may be correlated to a smaller surface concentration and not the initial boundary condition used as input to the model. Likewise, small differences at the higher z-values between the numerical and experimentally measured quantities for the other cases may also be a result of a slight time dependency in the measurements or could be a concentration build-up near the top of the wind tunnel during the experimental measurements. Since the top of the boundary layer above the surface lies at about 0.25 m, then dust concentrations that are consistently high relative to the numerical model lie either within the freestream or even within the boundary layer associated with the tunnel roof. For these reasons, the advective component could certainly be reduced and dust could accumulate near the top of the wind tunnel.

One of the greatest advantages of the numerical solution is it can be used to predict all the profiles from $x = 0.0$ m to $x = 5.0$ m. A general contour plot of this solution-type is shown in Fig. 6. Immediately, one notices that F_H, the Horizontal Flux of PM_{10}, levels off and does not linearly increase without bound. The emission rate is not a constant, but depends on the measuring locations along the fetch for the "steady-state" conditions. For instance, the numerical predictions indicate slightly higher emission rates at $x = 2.65$ m than at the $x = 4.38$ m for the constant surface boundary conditions. This phenomenon was witnessed in the experimentally measured emission rates as well. F_H the Horizontal Flux increases continuously, but not linearly, because the change in horizontal flux at long

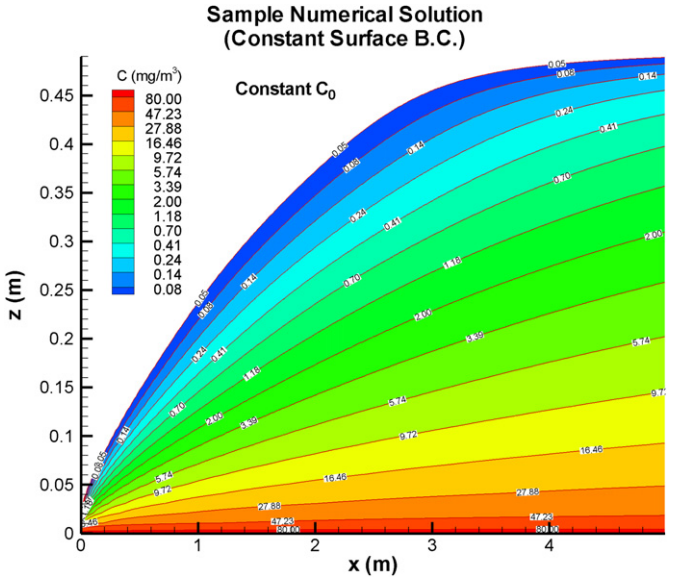

Fig. 6. Concentration contours of the numerical solution for the case in which the surface boundary condition is constant, $F(x) = C_0$. The domain of the wind-tunnel testing section is shown for the specific case where $u_* = 0.80$ m s^{-1}, $z_0' = 0.00063$ m, and $C_0 = 92.0$ mg m^{-3}.

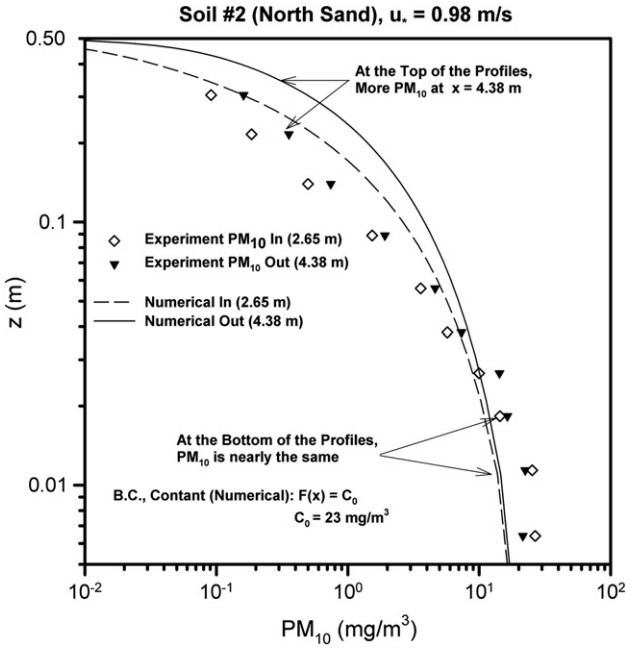

Fig. 7. Concentration profiles for high u_* values at $x = 2.65$ m and $x = 4.38$ m compared to numerical results for the same case.

enough fetches is only slightly perturbed by additions of dust from the surface. Likewise, the flux of dust decreases due to the near-surface vertical concentration gradient decreasing with increased fetch. The analysis thus far only considers the PM_{10} (soil and dust) sheared off the surface and advected; however, in the saltating arrangement there are much larger airborne particles being advected down the tunnel possibly further suppressing the near-surface PM_{10} flux, or quite the opposite, even bigger particles may be "splashing" PM_{10} off the surface. These phenomena may be addressed with different types of boundary conditions.

If $F(x)$ is taken as constant, the portions of the numerical concentrations profiles nearest the surface should converge at downstream fetch locations, $x = 2.65$ m and at $x = 4.38$. If the shear is significant (usually due to strong advective wind) then vertical turbulent diffusion is enhanced and the two concentration profiles could converge at multiple heights due to the enhanced mixing earlier in the fetch. A prediction of the profiles at the two different locations where there is both high initial shear and strong advection is compared to a similar experimental case in Fig. 7. Depending on the precision of the experimental testing method, these two profiles could prove to be identical, and measuring an emission rate between two probes spaced a couple meters apart would be difficult. In the experimental testing, this same conclusion was reached and emission rates were only calculated for the individual soils from the beginning of the fetch to the probe locations. In this case, the numerical prediction helps confirm the techniques that were used in the measurements.

Finally, the numerical F_H Horizontal Flux was plotted for different u_* as a function of the fetch length and compared to similar experimental results. An example comparison is shown in Fig. 8. The trends are similar between the numerical and experimental results; however, the fall-off of emissions is not predicted with the numerical model when applying constant surface boundary condition. The constant surface boundary condition does not account for possible near-surface "saturation" (mass loading). However, the constant surface boundary condition appears to be a fair representation of the emission processes during steady-state erosion as the experimental and numerical comparisons proved to be well correlated for the "loose soil" emissions cases.

4.4. Surface boundary condition, step function

The numerically predicted fetch effect for the step-function simulation was plotted with the experimental data. An example of this comparison for the North Sheet simulation is given in Fig. 9. The plot shows an abrupt change where there is a transition from a less emissive soil to a more emissive soil. When the South Sheet simulation was compared to the experimental results, the difference in emissions between the sand and the loamy soil is less obvious, but present. The step-function boundary conditions were

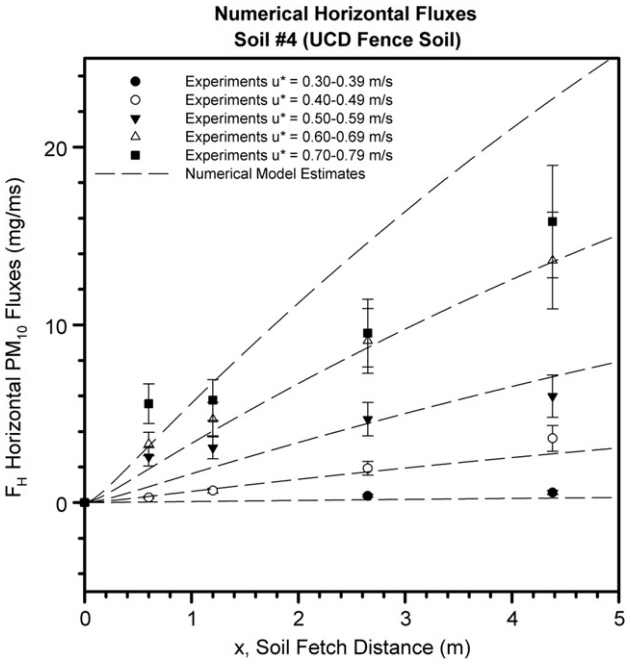

Fig. 8. Comparison of experimental and numerical F_H Horizontal Flux of PM_{10} for Soil #4 for multiple friction velocities u_* at different fetch locations.

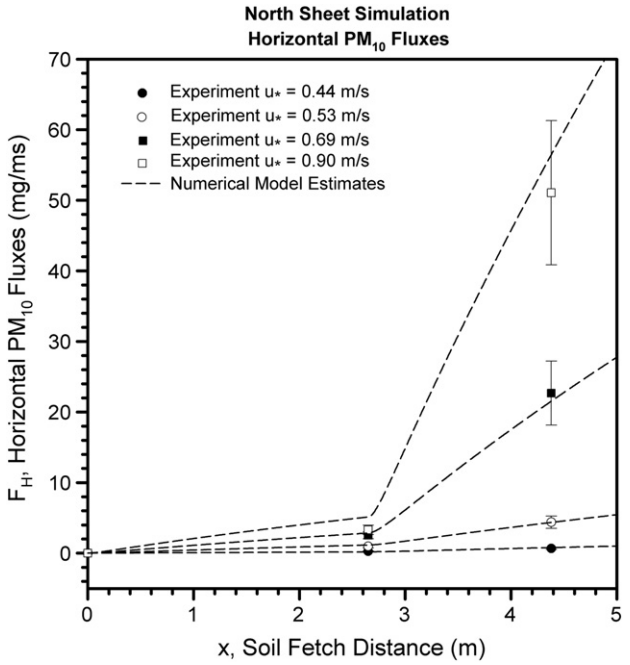

Fig. 9. Comparison of experimental and numerical F_H Horizontal Flux of PM_{10} for multiple friction velocities u_* at different fetch locations for the North Sheet Simulation.

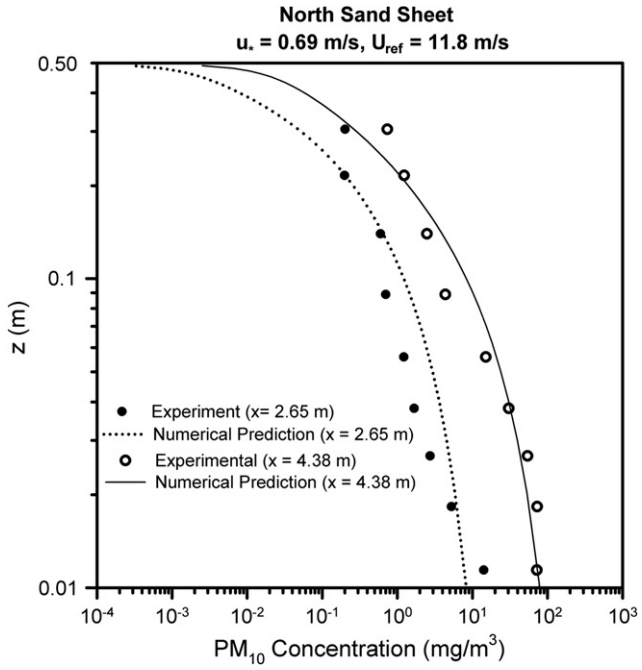

Fig. 11. Comparisons of the numerical and experimental concentration profiles for the North Sheet Simulation.

estimated from the experimental results. The comparison is quite close indicating the step-function boundary condition is a reasonable assumption for the wind-tunnel experimental physics where there is a transition between two different soils. A complete solution of the fetch effect is given for one of the North Sheet Simulation cases in Fig. 10. Representative numerical concentration profiles for this case are also shown in Fig. 11 with the corresponding experimental result. The numerical prediction compares well with the experimental horizontal fluxes and concentration profiles. The step-function solution is a boundary condition that does not readily lend itself to analytical solution; and, thus, this case exemplifies the advantages of numerical solution. The experimental results and the numerical solutions also show the applicability of partitioning a dust source into regions with different surface boundary conditions to give estimates of the total emissions.

4.5. Surface boundary condition, exponential function

A full solution for $\alpha = -0.50$ for the exponential boundary condition is given in Fig. 12. Near the surface, the concentrations drop significantly as the fetch increases. This decrease becomes

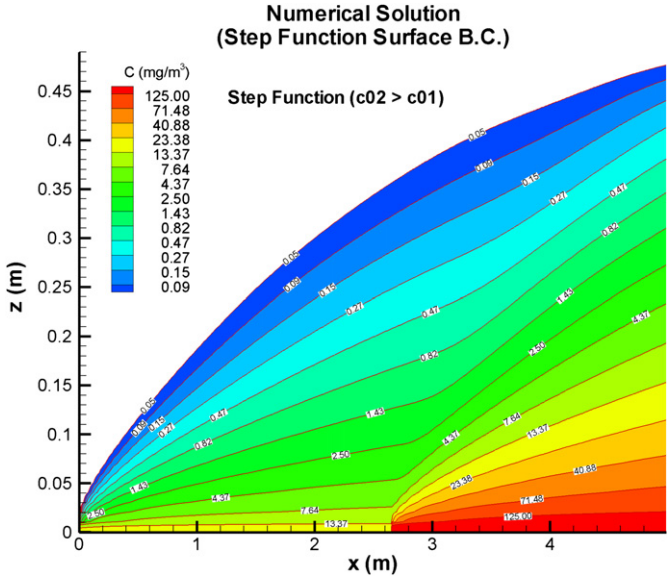

Fig. 10. Concentration contours of the numerical solution for the case in which the surface boundary condition $F(x)$ is a step function. The domain of the wind-tunnel testing section is shown for the specific case where $u_* = 0.90$ m s^{-1}, $z_0' = 0.000673$ m, $C_{01} = 20.0$ mg m^{-3}, and $C_{02} = 300.0$ mg m^{-3}.

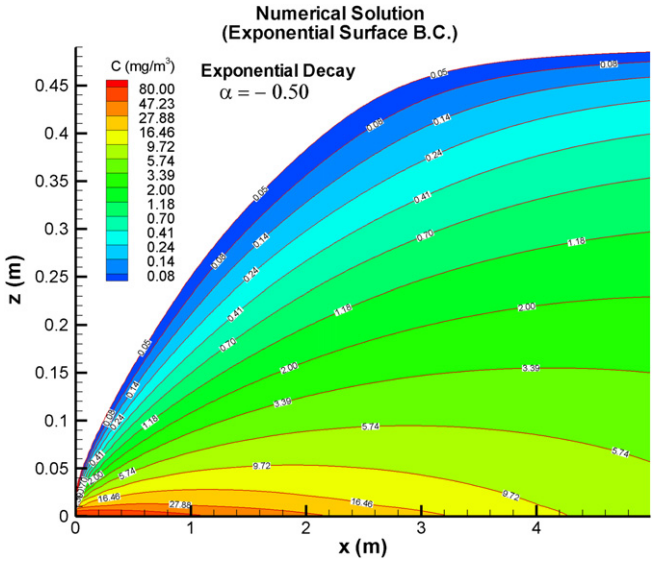

Fig. 12. Concentration contours of the numerical solution for the case in which the surface boundary condition $F(x)$ is exponentially decaying. The domain of the wind-tunnel testing section is shown above for the specific case where $u_* = 0.80$ m s^{-1}, $z_0' = 0.001$ m, $C_0 = 80.0$ mg m^{-3}, and $\alpha = -0.50$.

more significant as α become increasingly negative. The numerical input conditions were matched to an experimental case in which exponential decay of the surface boundary condition was suspected. The numerical solution profiles for this case were calculated for $x = 2.65$ m and $x = 4.38$ m and compared to the experiments as shown in Fig. 13. At the downwind location in both the numerical and experimental concentration profiles, the near-surface concentrations are lower than upwind. Also, it is worthwhile to note that this crossing phenomenon is seen experimentally in each of the four soils at the higher u_* values. At these values the suspended mass is large and the exponential form of the boundary condition may describe the physics of the experimental surface in a qualitative sense in which mass loading is effecting entrainment of dust. True α values could be determined from methodical experiments at the very highest u_* values for each soil.

Lastly, the horizontal PM_{10} fluxes are plotted as a function of the wind-tunnel fetch for $\alpha = 0.0$, $\alpha = -0.25$ and $\alpha = -0.50$ in Fig. 14. The horizontal flux of PM_{10} decreases for increasing negative α values in this plot. Drops in the horizontal flux are observed between $x = 2.65$ m and $x = 4.38$ m for $\alpha = -0.50$: this was also observed in some of the wind-tunnel experimental tests. The decaying exponential boundary conditions compare well qualitatively with some of the higher velocity experimental testing and may describe the physics of the lower boundary condition under increasing suspended mass along the length of the fetch. Further studies are needed to verify this result; however, the preliminary comparisons are promising.

4.6. Surface boundary condition, sinusoidal function

Numerical cases for the sinusoidal boundary condition were examined for $\lambda_r = 0.2$ m, $\lambda_r = 0.5$ m, and $\lambda_r = 2.0$ m. The domain of the wind-tunnel testing section is shown for the specific case where $u_* = 0.80$ m s^{-1}, $z_0' = 0.001$ m, and $C_0 = 80.0$ mg m^{-3}, and one of the resulting numerical solutions is shown in Fig. 15 for $\lambda_r = 0.2$ m. For these cases with simulated ripple beds, as λ_r increases the perturbation of the concentration away from the surface becomes greater; however, the horizontal fluxes remain essentially the same as shown in Fig. 16. This analysis assumes ripples with unappreciable heights such that the ridges do not alter the flow significantly. These types of ripples were seen in the wind-tunnel experiments after an initial sorting. The effect of the ripple formation is to decrease the emissions over that of a "purely" flat surface with no ripples ($F(x) = C_0$) as shown in Fig. 16. The decrease in emissions is attributed to the decrease in surface area subject to PM_{10} erosion. A numerical solution of this type provides support that a decrease in emissions should be seen when one transitions from the flat unsorted surface to "steady-state" ripples. In the experiments, when a concentration probe was held near the

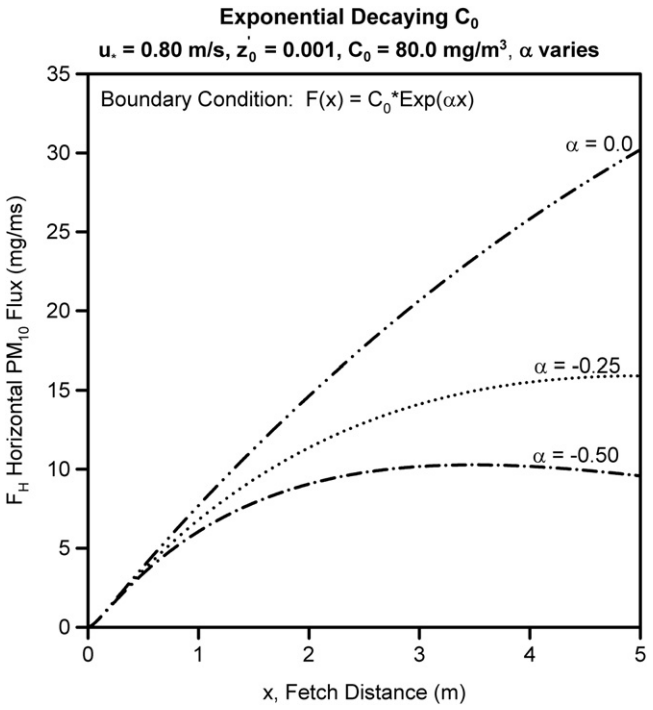

Fig. 14. Horizontal PM_{10} Flux F_H for different values of α in the exponentially decaying boundary condition. For this case $u_* = 0.80$ m s^{-1}, $z_0' = 0.001$ m, $C_0 = 80.0$ mg m^{-3}, and $\alpha = 0.0$, $\alpha = -0.25$, and $\alpha = -0.50$.

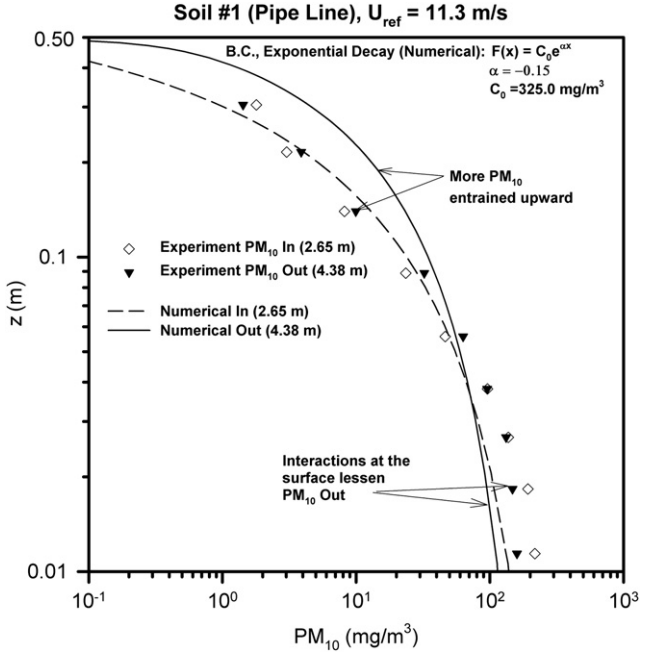

Fig. 13. Concentration profiles for the numerical solution with exponential decaying surface boundary condition compared with the same experimental case at two fetch locations $x = 2.65$ m and $x = 4.38$ m.

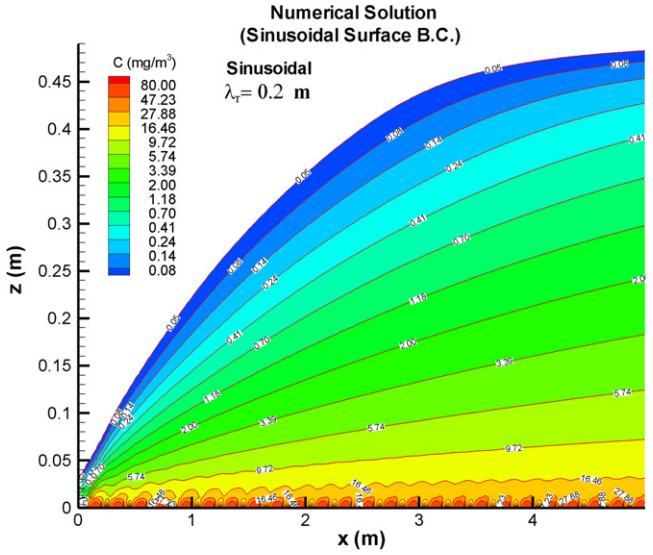

Fig. 15. Contour plots for sinusoidal boundary conditions for $\lambda_r = 0.2$ m.

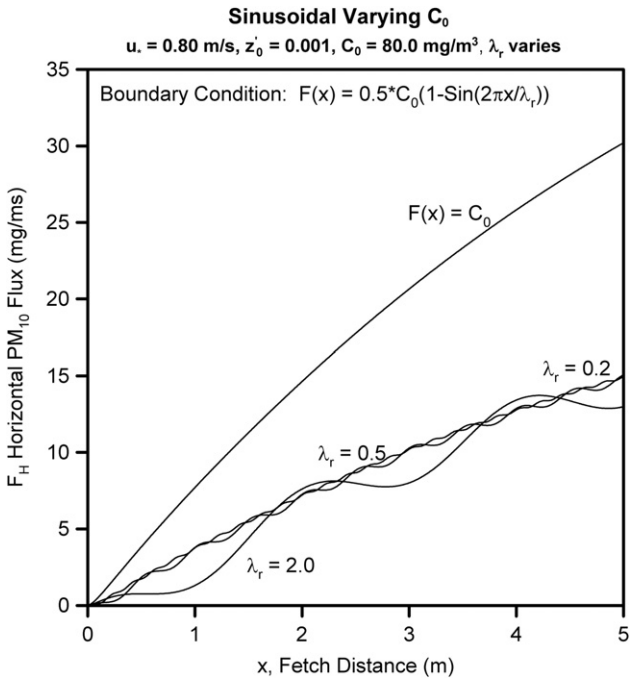

Fig. 16. Horizontal PM_{10} Flux for different sinusoidal boundary conditions representing ripple effects, and for a flat surface $F(x) = C_0$.

surface, a drop in emissions was observed during the transition from the flat eroding surface to the ripple-filled "steady-state" eroding surface.

4.7. Surface boundary condition, combined functions

Finally, a single combined exponential and sinusoidal boundary condition was formed and the numerical equations solved. A solution for this type of boundary conditions is shown in Fig. 17 for $\alpha = -0.25$ and $\lambda_r = 0.2$ m. The solution gives results similar to those shown in Fig. 13 for the concentration profiles. These results are experimentally similar to the data for higher u_* values. Thus, it is possible that this type of boundary condition is representative of the "steady-state" erosion in all the experiments at the higher u_* values. A recalibration of the input surface boundary conditions for the model may provide better comparison with the experimental data. However, this exercise is left for another study.

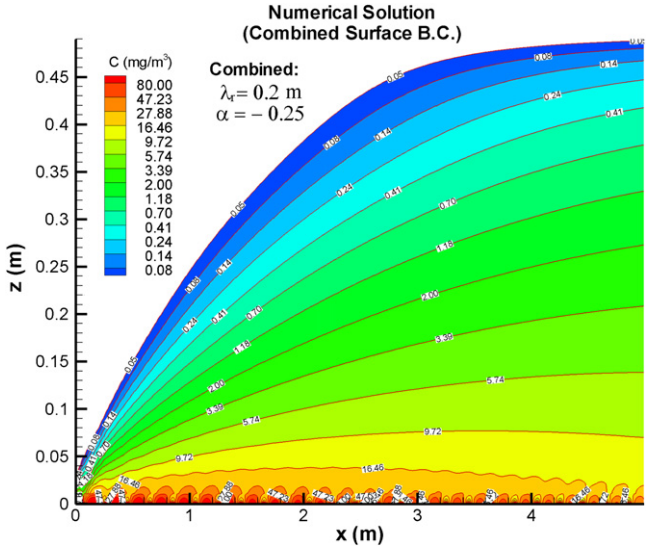

Fig. 17. Numerical solution for the combined sinusoidal and exponential boundary condition. The domain of the wind-tunnel testing section is shown above for the specific case where $u_* = 0.80$ m s^{-1}, $z_0' = 0.001$ m, $C_0 = 160.0$ mg m^{-3}, $\alpha = -0.25$, and $\lambda_r = 0.2$ m.

5. Conclusions

"Simple" predictive mathematical and numerical models that simulate the physics of advection–diffusion of dust in a wind tunnel were studied and compared to wind-tunnel results. The novel aspects of this study include: comparison of concentration profiles of dust obtained experimentally in the wind tunnel with those calculated numerically; comparison of the calculated numerical fetch effect on dust emissions with that obtained in the wind tunnel; and comparison of the emission rates calculated numerically with those obtained experimentally in the wind tunnel. In addition, an analysis of the surface boundary condition effect on the numerical solution and how those effects might explain different experimental results was performed.

The constant concentration surface boundary condition appears to be a fair representation of the emission processes during steady-state erosion as the experimental and numerical comparisons proved to be well correlated for the loose soil emissions cases. The concentration boundary conditions were established empirically, and emphasize importance of wind-tunnel studies in obtaining data for model input. The concentration profiles as well as the fetch-effect results both compared well for these cases. The numerically produced fetch-effect emission results show that the horizontal dust flux does not increase linearly without bound; and, therefore, the emission rate calculation can be biased by the length of the soil bed over which an emission rate is calculated. This same result was observed experimentally in Roney and White (2006). More elaborate boundary conditions were explored to possibly explain other physical phenomena observed in the wind-tunnel emission studies such as step jumps in surface types, near-surface mass loading, and rippling of the surface.

The numerical prediction of the experimental North and South Sheet simulation emissions results were also successful when a step-function surface boundary condition was applied. Horizontal fluxes as well as concentration profiles compared qualitatively with the experimental data. The step-function solution is a boundary condition that does not readily lend itself to analytical solution, and thus, exemplifies the advantages of numerical solution. The decaying exponential boundary conditions which could represent extreme mass loading at the surface–air interface compared well qualitatively with some of the higher velocity experimental results. Further studies are needed to verify this result; however, the preliminary comparisons are promising. A sinusoidal boundary condition was explored to represent the ripple bed cases. The numerical results for this case show decreases in emissions which can be attributed to the decrease in surface area subject to PM_{10} erosion. This solution provides additional support that a decrease in emissions should be seen when one transitions from the flat loose erodible surface to the "steady-state" rippled surface in the experiments. Lastly, these two boundary conditions, exponential and sinusoidal, were combined, providing a numerical solution that is reasonable representation of the "steady-state" erosion as well.

In all, two-dimensional steady-state solutions of the advection–diffusion equation were explored and compared to the wind-tunnel results for dust PM_{10} emissions and concentration profiles, yielding reasonable correlation between the two. Though the approach is "simple" (a complete time dependent three-dimensional solution is not attempted), the numerical results combined with the experimental results provide an invaluable foundation

upon which more "complicated" models can be developed to assess fugitive dust from erodible surfaces.

Acknowledgments

The California Air Resources Board (CARB) funded parts of this research under the Interagency Agreement 97-718. In addition, the Great Basin Unified Air Pollution Control District (GBUAPCD) was supportive of this research effort and granted access to Owens (dry) Lake.

References

Bagnold, R.A., 1941. The Physics of Blown Sand and Desert Dunes. Chapman and Hall, Ltd., London.

Eltayeb, I.A., Hassan, M.H.A., 1992. Two-dimensional transport of dust from an infinite line source at ground level. Geophysical Journal International 110, 571–576.

Gillette, D., Goodwin, P., 1974. Microscale transport of sand-sized soil aggregates eroded by wind. Journal of Geophysical Research 79, 4080–4084.

Hassan, M.H.A., Eltayeb, I.A., 1991a. Suspension transport of wind-eroded sand particles. Geophysical Journal International 104, 147–152.

Hassan, M.H.A., Eltayeb, I.A., 1991b. Time-dependent transport of dust. Journal of Geophysical Research 96 (D5), 9337–9339.

Hassan, M.H.A., Eltayeb, I.A., 1993. Two-dimensional transport of dust from an infinite line source at ground level: non-zero roughness height. Geophysical Journal International 115, 211–214.

Jacobson, M.Z., 1999. Fundamentals of Atmospheric Modeling. Cambridge University Press.

Pasquill, F., 1962. Atmospheric Diffusion. D. Van Nostrand, Princeton, NJ.

Pye, K., Tsoar, H., 1990. Aeolian Sand and Sand Dunes. Unwin Hyman, London, Boston.

Roney, J.A., White, B.R., 2006. Estimating fugitive dust emission rates using an environmental boundary layer wind tunnel. Atmospheric Environment 40, 7668–7685.

Roney, J.A., White, B.R., 2004. Definition and measurement of dust aeolian thresholds. Journal of Geophysical Research, Earth Surface 109, F01013.

Seinfeld, J.H., Pandis, S.N., 1998. Atmospheric Chemistry and Physics: From Air Pollution to Climate Change. John Wiley and Sons, Inc.